doi: 10.82124/CEAS-GNC-2026-059 CEAS-GNC-2026-059

Flight Test Based System Identification of an Unmanned Fixed-Wing Aircraft

Antonia Franke Student, Technische Universität Dresden, Chair of Flight Mechanics and Control, Dresden, Germany. antonia.franke@mailbox.tu-dresden.de

Martin Guist Research Assistant, Technische Universität Dresden, Chair of Flight Mechanics and Control, Dresden, Germany. martin.guist@tu-dresden.de

Sabine Wisbacher Research Assistant, Munich University of Applied Sciences HM, Munich, Germany. sabine.wisbacher@hm.edu

Daniel Ossmann Professor, Munich University of Applied Sciences HM, Munich, Germany. daniel.ossmann@hm.edu

Harald Pfifer Professor, Technische Universität Dresden, Chair of Flight Mechanics and Control, Dresden, Germany. harald.pfifer@tu-dresden.de

ABSTRACT

This paper presents the setup and results of a flight test campaign performed to identify the longitudinal motion of a small unmanned fixed-wing aircraft. The flight test experiments include manoeuvres to excite short-period and phugoid dynamics, as well as gliding flights to determine drag coefficients. Frequency ranges of the manoeuvre inputs are selected based on the dynamics of an initially derived linear approximation of the aircraft dynamics using aerodynamic vortex lattice method computations. By applying grey-box system identification, the corresponding aerodynamic parameters are estimated from recorded measurement data. The gathered results indicate satisfactory correlation with the mathematical modelling of the aircraft. This not only enables the development of suitable model-based control algorithms but also validates the entire mathematical model development chain for small fixed-wing unmanned aerial vehicles, i.e., from the initial approximation to flight test validation.

Keywords: System Identification, Flight Test, Small fixed-wing UAV

1 Introduction

Unmanned Aerial Vehicles (UAV) are used in a wide range of civil and military applications due to their versatility, endurance, and operational flexibility. UAVs with fixed wings that can carry larger payloads over long distances are particularly suitable for searching vast areas, supplying crisis regions, or last-mile logistics [1]. These application areas however also introduce individual challenges. Especially operations in urban areas impose high safety demands on flying vehicles. Narrow flight corridors between buildings and changing atmospheric wind fields present additional challenges for the operation of small UAVs, whose flight performance is easily affected by disturbances due to their low cruise speeds. Reliable control of these vehicles is essential to guarantee the successful completion of their missions. Developing such control systems requires a precise mathematical representation of the unmanned flight system to

Except where otherwise noted, content of this paper is licensed under a Creative Commons Attribution 4.0 International License.

The reproduction and distribution with attribution of the entire paper or of individual pages, in electronic or printed form, including any material under non-CC-BY 4.0 licenses is hereby granted by the authors and respective copyright owners.

enable high-performance control designs and high-fidelity nonlinear simulations. The performance of the control system strongly depends on the accuracy of the aerodynamic coefficients available in the models. To determine the mathematical model of an aircraft system, analytical or experimental methods can be applied. Models for UAVs usually rely on rough estimates of the flight dynamics via mathematical methods. Flight-testing to update the parameters is rarely performed simply due to cost and tie constraints during the development. Using appropriate flight test setups together with grey-box system identification methods allows an efficient way to update the initially derived models [2]. The mathematical model's parameters are adjusted using the input and output data measured during test flight. Reliable data generation during these test flights is enabled via adequate manoeuvre design in order to ultimately extract the aircraft's system dynamics.

This paper presents a lean system identification approach applied to the longitudinal dynamics of a small fixed-wing aircraft, taking into account their specific characteristics. Given the importance of the short-period dynamics for control design, this paper focuses on their identification through grey-box identification techniques. In addition, the phugoid mode is identified through the Transient Peak Ratio (TPR) approach, and steady-state flight tests are performed to estimate the glide ratio and drag coefficients. Beyond the specific results obtained for the investigated aircraft, this work provides a structured identification workflow for small UAVs with limited resources. The proposed approach demonstrates how typical challenges - such as missing onboard instrumentation for direct measurement of angle of attack or elevator deflection, and limited airspace for flight test manoeuvres - can be systematically addressed through appropriate model formulation, experiment design and signal selection.

There are several works dealing with aircraft system identification in the literature. A well-established overview for methods in the time-domain is provided in [3], while [4] covers approaches in frequency-domain. The literature on system identification specially for small fixed-wing aircraft is not as well developed. A survey on the application of system identification methods to small UAVs, including rotary and fixed-wing drones, is provided in [5], while [6] explicitly focuses on fixed-wing UAV system identification approaches via flight testing. The challenges connected to the identification of UAVs and strategies for addressing them are highlighted, e.g., in [7] and in [8]. In more detail, [9] presents the application of the output error method in time domain to derive an aerodynamic model from flight test data covering longitudinal and lateral dynamics. In [10] a two step identification approach for a small UAV first determines a nonlinear model structure and then identifies the corresponding aerodynamic parameters from flight tests. In contrast, [11] deals with the application of system identification methods using unplanned, operational flight data when no dedicated test data are available.

The use of grey-box system identification methods, however, initialised with parameters from mathematical models which are derived from aerodynamic computations, is limited. Thus, based on mathematical descriptions of the aircraft dynamics, detailed in Section 2, together with gathered parameter initialisations from aerodynamic computations, a specially tailored flight test setup is presented in Section 3. This enables a flight test campaign, which allows parameter updates around the expected frequencies of the aircraft's eigenmodes using well-established excitation signals from [3]. The results, detailed in Section 4, describe the identification of the short-period dynamics, which are determined separately from the phugoid motion using a grey-box approach [12]. Identification of the phugoid motion via the TPR [13] and steady aircraft performance tests to obtain glide number and drag coefficients finally provide the required insight into the overall longitudinal aircraft dynamics to enable advanced control design methods in the future.

2 Identification Methodology

In this work, the longitudinal motion of the test aircraft is analysed in a flight test campaign including multiple flights to excite short-period and phugoid motion, and to approximate drag during gliding. The

Except where otherwise noted, content of this paper is licensed under a Creative Commons Attribution 4.0 International License.

The reproduction and distribution with attribution of the entire paper or of individual pages, in electronic or printed form, including any material under non-CC-BY 4.0 licenses is hereby granted by the authors and respective copyright owners.

short-period motion is a fast, strongly damped rotational oscillation about the pitch axis dominating the aircraft's longitudinal dynamics over short time intervals. In contrast, the phugoid dynamics evolve over longer timescales as a slowly damped flight-path oscillation. To enable a reliable system identification, the different longitudinal modes are excited independently by suitable manoeuvres, allowing a clear separation of the respective aircraft responses. From a trimmed state, the short-period motion is usually excited by a multistep elevator deflection, while the phugoid mode can be excited by an elevator pulse [3]. For flight control design purposes, the identification of the short-period mode is particularly important, as its fast dynamics introduce higher complexity in the control task. Therefore, this work focuses on the identification of the aerodynamic parameters describing the short-period motion. The subsequent analysis of the phugoid manoeuvres and gliding flights complements the overall characterisation of the longitudinal aircraft's motion. A detailed description of the mathematical methods and identification approaches for the different sub-tasks is provided in this section.

2.1 Grey-Box Identification for Short-Period Dynamics

For the identification of the short-period dynamics of the UAV under study, a grey-box model is applied. The underlying model is linear time-invariant (LTI) and can be written in state-space form simply by

$$\begin{aligned} \dot{x}(t) &= Ax(t) + Bu(t) \\ y(t) &= Cx(t) + Du(t) \end{aligned} \tag{1}$$

with the n-dimensional state vector $x(t) \in \mathbb{R}^n$, the p-dimensional input vector $u(t) \in \mathbb{R}^p$, the q-dimensional output vector $y(t) \in \mathbb{R}^q$ and the corresponding state-space matrices $A \in \mathbb{R}^{n\times n}$, $B \in \mathbb{R}^{n\times p}$, $C \in \mathbb{R}^{q\times n}$, and $D \in \mathbb{R}^{q\times p}$. Its response to a given input signal is compared to the observed behaviour of the system. The aim is to minimise the error between the measured flight test data and the predicted model response [12]. Starting from an initial guess, or, as done in this paper, from a-priori performed aerodynamic computations, the parameters of the model are iteratively adjusted. To solve the described optimisation problem, the function *greyest* implemented in the MATLAB System Identification Toolbox is used. In each iteration, it evaluates different search methods, such as subspace Gauss-Newton, Levenberg-Marquardt and steepest descent least-squares search, and the first search result yielding a reduction in the prediction error is adopted. The algorithm is chosen for its numcerical efficiency which ensures rapid convergence while maintaining low computational cost.

In this work, the following well-established linear state-space model is formulated to describe the short-period dynamics [14]. The state vector contains the angle of attack α and the pitch rate q, while the input is the elevator deflection δ_e (with positive δ_e defined as downward deflection), leading to the state-space-description

$$\begin{bmatrix} \dot{\alpha} \\ \dot{q} \end{bmatrix} = \begin{bmatrix} Z_\alpha & Z_q + 1 \\ M_\alpha & M_q \end{bmatrix} \begin{bmatrix} \alpha \\ q \end{bmatrix} + \begin{bmatrix} Z_{\delta_e} \\ M_{\delta_e} \end{bmatrix} \delta_e. \tag{2}$$

The vertical acceleration in body axes $a_{z,CG}$ and the pitch rate q are considered as the outputs of the system and related to the states via the output equation given by

$$\begin{bmatrix} a_{z,CG} \\ q \end{bmatrix} = \begin{bmatrix} Z_\alpha V^* & Z_q V^* \\ 0 & 1 \end{bmatrix} \begin{bmatrix} \alpha \\ q \end{bmatrix} + \begin{bmatrix} Z_{\delta_e} V^* \\ 0 \end{bmatrix} \delta_e. \tag{3}$$

Except where otherwise noted, content of this paper is licensed under a Creative Commons Attribution 4.0 International License.

The reproduction and distribution with attribution of the entire paper or of individual pages, in electronic or printed form, including any material under non-CC-BY 4.0 licenses is hereby granted by the authors and respective copyright owners.

The model in Eq. (2) and Eq. (3) depends on the aerodynamic force derivatives Z_i and moment derivatives M_i with $i \in \{\alpha, q, \delta_e\}$, i.e.,

$$\begin{aligned} Z_\alpha &= -\frac{\overline{q}^* S}{V^* m} c_{L\alpha}, & M_\alpha &= \frac{\overline{q}^* S c}{I_{yy}} c_{M\alpha}, \\ Z_q &= -\frac{\overline{q}^* S}{V^* m} c_{Lq}, & M_q &= \frac{\overline{q}^* S c}{I_{yy}} c_{Mq}, \\ Z_{\delta_e} &= -\frac{\overline{q}^* S}{V^* m} c_{L\delta_e}, & M_{\delta_e} &= \frac{\overline{q}^* S c}{I_{yy}} c_{M\delta_e}, \end{aligned} \tag{4}$$

which are functions of the aircraft characteristics, the selected trim point, and the coefficients c_{Li} and c_{Mi} to be estimated. In more detail, the derivatives in Eq. (4) depend on the known dynamic pressure $\overline{q}^*$, wing area S, chord length c, aircraft mass m, the aircraft's moment of inertia I_{yy} about the pitch axis, and the trim airspeed V^*. Using grey-box identification, the aircraft dynamics in Eq. (2) are identified for trim-conditions in steady, horizontal flight. Thus, a set of linear models each of the form in Eq. (2) is derived, which covers the normal operational flight range of the aircraft.

2.2 Phugoid Motion Characterisation via Transient Peak Ratio

As this work focuses on the identification of the aerodynamic parameters describing the short-period dynamics for flight control design purposes, the in-flight excited phugoid motion is analysed only in terms of its frequency and damping using the TPR method. The TPR is defined as the ratio of two consecutive peak amplitudes, i.e., z_i and z_{i+1}, of an oscillation signal occurring at intervals equal to the oscillation period T. Assuming that the oscillation decreases exponentially, the damping ratio ζ is described as a function of this TPR [13]. In combination with the oscillation period, the natural frequency ω_n of the observed oscillation can be determined. Finally, ω_n and ζ are given by

$$\omega_n = \frac{2\pi}{T\sqrt{1-\zeta^2}} \quad \text{and} \quad \zeta = \frac{1}{\sqrt{1 + \left(\frac{\pi}{\ln|\mathrm{TPR}|}\right)^2}}, \tag{5}$$

with $\mathrm{TPR} = z_{i+1}/z_i$. This method provides insights into the frequency and damping of a measured oscillation signal even if only a few cycles are recorded.

2.3 Estimation of Drag Coefficient from Gliding Flights

In addition to the investigation of the UAV's dynamic behaviour, valuable performance information is obtained by analysing its steady-flight characteristics. During steady gliding flight, the well-known relationship

$$E = \frac{c_L}{c_D} = \frac{1}{\tan \gamma_{\text{glide}}} \tag{6}$$

link the glide ratio E with the glide angle γ_{glide} as well as lift c_L and drag c_D coefficients. These relationships can be used to determine drag coefficients as a function of the angle of attack. The drag coefficient results from Eq. (6) by

$$c_D = \frac{2mg \sin \gamma_{\text{glide}}}{\rho V^2 S} \tag{7}$$

with the glide angle γ_{glide}. Depending on the aircraft configuration, however, this method cannot be used to exactly derive the required lift and drag coefficients for the mathematical model. This is, e.g., due to

Except where otherwise noted, content of this paper is licensed under a Creative Commons Attribution 4.0 International License.

The reproduction and distribution with attribution of the entire paper or of individual pages, in electronic or printed form, including any material under non-CC-BY 4.0 licenses is hereby granted by the authors and respective copyright owners.

the lack of foldable propellers and the thereby additionally induced drag during gliding - simply as the propeller continues to rotate at idle speed. Under normal operating conditions, however, this does not occur and should therefore not be taken into account in aircraft modelling. Nevertheless, the method is highly valuable for estimating the remaining gliding distance in the event of an engine failure, and thus plays an important role in the design of appropriate safety measures.

3 Flight Test Setup

To obtain the data required for identifying the longitudinal flight characteristics of the test vehicle a series of experiments are carried out at the airfield of the Model Flying Club TU Dresden (N 50° 58.428' E 13° 44.712', H = 334 m). This section provides details on the aircraft setup and the design of the overall flight campaign.

3.1 Test Vehicle and Instrumentation

The fixed-wing UAV examined in this work is the Urban Condor X, depicted in Fig. 1. It is a modified version of a Sig Kadet LT-40 featuring a newly developed modular 3D-printed wing and an adapted fuselage design. The newly designed wing has an increased wingspan of 2 m and is been equipped with high-lift devices. The modified fuselage and tail unit are made from wood and 3D-printed components. The fuselage provides space to carry various electronic components and measuring instruments, which are mounted using 3D-printed fixtures. The tail unit is attached to the fuselage via a carbon fibre reinforced plastics spar. The modular design of the wing and fuselage enables straightforward adaptations to specific operational needs as well as fast repairs in the event of damage. The UAV is powered by a brushless electric motor with a single propeller. During the performed flight tests, the Urban Condor X has a weight of 7.6 kg. Its cruise speed is about 20 m/s and stall is reached at approximately 13 m/s.

A Pixhawk 6x flight control unit is used to enable fully autonomous operation via close-loop control algorithms as well as the execution of elevator commands for excitation purposes during the flight tests. It collects data from the internal Inertial Measurement Unit (IMU) at a sampling rate of 200 Hz, including the accelerometer, gyroscope and magnetometer. With the internal barometers and the temperature sensor the air density is calculated. In addition, a pitot static system is used to provide airspeed. The position of the vehicle can be tracked with a GPS sensor. All data are recorded on an SD card in log files. Using the RFD868x-EU telemetry system in combination with the QGroundControl interface, data are available in real time and selected control parameters can be adjusted online during flight.

Fig. 1 UAV Urban Condor X at the test airfield

3.2 Test Programme and Manoeuvre Design

The input signals to excite the longitudinal motion need to be designed to adequately stimulate the mode under investigation while minimising the excitation of other motions [3]. Initial estimates of the aerodynamic coefficients of the Urban Condor X are available from calculations with the Athena Vortex Lattice (AVL) aerodynamic analysis programme [15]. They enable the definition of an initial state-space model of the longitudinal motion. Based on this model, the natural frequencies of the longitudinal modes are determined and the aircraft response to specified manoeuvre inputs is simulated. This finally allows

Except where otherwise noted, content of this paper is licensed under a Creative Commons Attribution 4.0 International License.

The reproduction and distribution with attribution of the entire paper or of individual pages, in electronic or printed form, including any material under non-CC-BY 4.0 licenses is hereby granted by the authors and respective copyright owners.

to shape the input signal parameters for the flight tests with respect to size and duration of the control surface deflections. These signals are flashed onto the Pixhawk 6x flight control unit. A modular flight test setup allows to further adjust the signal parameters via telemetry link to the UAV during flight tests. This overall setup avoids cumbersome iterations and reduces the number of required flight tests.

Each manoeuvre is initiated at steady horizontal, wings-level flight of the aircraft at a specified trim speed. The experiments are performed at three different trim airspeeds, i.e, 15 m/s, 20 m/s, and 25 m/s, covering the main operational flight envelope of the aircraft. The lower airspeed bound ensures a sufficient margin above stall speed, while the upper bound is limited by increased power consumption reducing the available flight duration for manoeuvre execution. At the beginning of each flight, the required trim values for thrust and elevator deflection are adjusted manually via the QGroundControl interface, until steady horizontal flight is reached at the desired airspeed. To explicitly consider the pronounced atmospheric influences on small fixed-wing aircraft, each input signal is repeated at least three times. This also accounts for measurement variability due to the low-cost hardware. After each input signal, the UAV is allowed to oscillate freely before the next manoeuvre cycle begins. Between manoeuvres, the UAV is retrimmed to steady, horizontal flight to maintain constant reference conditions. The performed manoeuvres and the corresponding excitation signals are discussed in detail below, while an overview is provided in Table 1.

The first flight test scenario is designed to investigate the short-period motion of the aircraft. During the manoeuvres, thrust is assumed to be constant as the pulse width modulation (PWM) signal controlling the motor is not changed. Based on the preliminary aerodynamic computations, the short-period frequency of the Urban Condor X at its cruise speed of 20 m/s is estimated to be approximately $f_n = 1.4$ Hz. Thus, an appropriate input signal must cover frequencies around this frequency to sufficiently stimulate the dynamics of the system. The short-period motion is excited by deflecting the elevator using chirp and multistep 3211 inputs. The chirp input is a sinusoidal signal of the form

$$\Delta\delta_e(t) = A_{\text{chirp}} \sin\left(2\pi\left(f_{\text{start}}t + \frac{f_{\text{end}} - f_{\text{start}}}{2T}t^2\right)\right), \tag{8}$$

whose frequency increases linearly from the initial frequency f_{start} to the final frequency f_{end} over a defined period of time T at a constant amplitude A_{chirp}. To cover the relevant frequency range of the short-period motion, a start frequency of 0.5 Hz and an end frequency of 3 Hz are selected. Within this frequency range, the actuator is able to follow the elevator deflection command precisely. The signal duration is limited to 10 s, respecting the longest possible flight distance within the available airspace. The amplitude A_{chirp} of the chirp input is set to 10° around trim value of the elevator deflection. This amplitude ensures sufficient excitation energy of the short-period motion, but is still small enough to not deviate the aircraft significantly from the selected trim point.

The 3211 signal consists of four consecutive impulses with alternating positive and negative deflections of constant amplitude. The relative durations of the sections are 3, 2, 1, and 1 time steps, respectively. The time step needs to be chosen such that the frequency of the short-period mode to be identified is placed in the middle or upper third of the input signal frequency spectrum, see [3]. Based on the rule of thumb a time step $\Delta t \approx 0.3/f_n \approx 0.2$ s is selected. Likewise to the chirp signal, a reference amplitude of $A_{3211} = 10°$ is applied for the 3211 signal. In contrast to the original form described in [3], however, the amplitudes are varied to achieve a more uniform distribution of the frequency content around the expected short-period frequency. Thus, the first impulse reaches 67% of A_{3211}, the second impulse the full amplitude, and the two impulses at the end of the signal reach 92% of the reference amplitude A_{3211}. Herein, the chirp input signal is selected for the identification itself, as it ensures a sufficiently constant excitation across the frequency range of interest. Subsequently, the derived model of the short-period motion is validated with independent datasets generated using the 3211 excitation signal.

Except where otherwise noted, content of this paper is licensed under a Creative Commons Attribution 4.0 International License.

The reproduction and distribution with attribution of the entire paper or of individual pages, in electronic or printed form, including any material under non-CC-BY 4.0 licenses is hereby granted by the authors and respective copyright owners.

The second flight test scenario covers experiments to characterise the phugoid motion of the aircraft. The phugoid frequency of the Urban Condor X at its cruise speed is located in a low-frequency range around approximately 0.09 Hz, indicated by the preliminary aerodynamic analyses. During the performed flight tests, the phugoid motion is initiated by an elevator pulse. Its amplitude and duration are designed to deliver sufficient excitation to the system, while remaining within the actuator's capability to command the elevator deflection accurately. Accordingly, the pulse amplitude is set to $-30°$ with a duration of 0.5 s. For the test case of 25 m/s airspeed, the pulse duration is reduced to 0.3 s. Similarly to the short-period manoeuvres, constant thrust is assumed, as no change of the motor PWM signal is commanded.

In the last flight test scenario of the test campaign, steady gliding flights are performed to determine the drag coefficient as a function of the angle of attack. The motor is turned off while a constant elevator deflection is applied, and the resulting aircraft response is recorded for at least 10 s. To cover an angle of attack range corresponding to the examined trim speeds, elevator deflections between $-1°$ and $-12°$ are commanded.

Table 1 Performed manoeuvres with corresponding control inputs

Identification scenario	Control input	Elevator amplitude	Duration or timestep	Additional attributes
Short-period	Chirp	10°	$T = 10\,\text{s}$	$f_{\text{start}} = 0.5\,\text{Hz}$ $f_{\text{end}} = 3\,\text{Hz}$
Short-period	3211	10°	$\Delta t = 0.2\,\text{s}$	-
Phugoid	Pulse	−30°	$\Delta t = 0.5\,\text{s}$ (for 15 m/s, 20 m/s) $\Delta t = 0.3\,\text{s}$ (for 25 m/s)	-
Gliding flight	Step	$[-1°, -12°]$	at least 10 s	no thrust

4 Flight Test based System Identification

During the test campaign, 15 flights have been completed including multiple short-period, phugoid and gliding identification scenarios at reference airspeeds of 15 m/s, 20 m/s and 25 m/s. The flight tests were performed under calm atmospheric conditions, with no noticeable gusts or thermals. This section provides the results of the data analyses used to characterise the longitudinal dynamics of the Urban Condor X.

4.1 Flight Test Data Processing

The recorded data include time series of airspeed, altitude, accelerations, pitch rate, pitch angle and elevator commands. To investigate accelerations and angular rates, the raw measurement data from the IMU is used, while the analysed measurements for airspeed and pitch angle rely on data processed by the Pixhawk firmware including an internal Extended Kalman Filter. To ensure the validity of the datasets used for system identification, acceptance criteria are applied to the recorded flight manoeuvres. For the short-period datasets, only manoeuvres with a maximum deviation of 2 m/s around the trim airspeed are included. The phugoid characterisation relies on datasets in which the total loss of altitude is limited to 1 m by the end of the manoeuvre. Furthermore, data analysis and post-processing are carried out to reduce the influence of measurement noise. To determine whether the measurements are suitable for

Except where otherwise noted, content of this paper is licensed under a Creative Commons Attribution 4.0 International License.

The reproduction and distribution with attribution of the entire paper or of individual pages, in electronic or printed form, including any material under non-CC-BY 4.0 licenses is hereby granted by the authors and respective copyright owners.

system identification their frequency content as well as the coherence spectra

$$K_{uy}(\omega) = \sqrt{\frac{\Phi_{uy}^2(\omega)}{\Phi_{uu}(\omega)\Phi_{yy}(\omega)}}, \tag{9}$$

of the measurements with the input signal is evaluated. In Eq. (9), Φ_{uy} is the cross-correlation spectrum and Φ_{uu} and Φ_{yy} are the auto-correlations of the input signal u and the output signal y, respectively [12].

The identification of the short-period dynamics relies on pitch rate, vertical acceleration in body axes, and pitch acceleration. While the first two are directly measured, the latter is calculated by numerical differentiation using the central difference for interior points and single-sided differences for the boundary points of the recorded data series. These datasets together with the input signals are evaluated with respect to frequency content and coherence spectra to determine their adequacy for the identification. The datasets generated by the chirp and 3211 inputs show the expected dominant frequency content within the excitation profile of the input signal, indicating that the eigenmodes of the aircraft have been sufficiently excited. Analysing the coherence spectra (Eq. (9)) of the available datasets indicates that coherence values between the elevator input signals and the output signals are close to one within the frequency range of interest for short-period motion. This is illustrated in Fig. 2 for pitch rate datasets at the three considered airspeeds of 15 m/s (——), 20 m/s (——) and 25 m/s (——). The vertical and pitch acceleration datasets show similar coherence spectra. The analysis of both the frequency content and the coherence spectra finally confirms that the collected datasets are suitable for the identification of the aircraft's short-period motion.

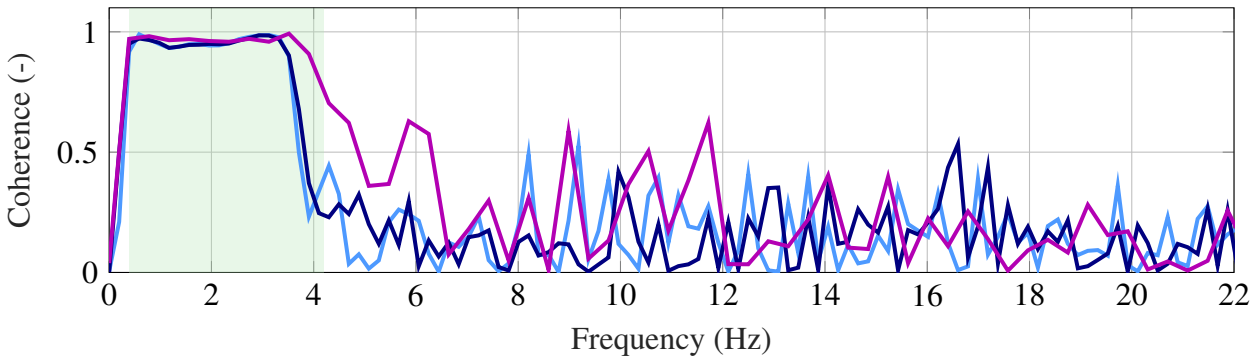

Fig. 2 Pitch rate coherence spectra for chirp excitation at airspeed of 15 m/s (——), 20 m/s (——) and 25 m/s (——)

Signal components outside the frequency range of high coherence provide little meaningful information for system identification and are predominantly affected by noise. To reduce the influence of noise, a 5$^{\text{th}}$-order digital butterworth filter is applied. Since the measurement data are passed through the filter in both forward and reverse direction, there is no phase shift. Due to the selected excitation frequency range of the chirp signals, a cut-off frequency of 6 Hz is selected at an airspeed of 15 m/s, while a cut-off frequency of 8 Hz is used for higher airspeeds. In addition, the measurement data are centred around zero based on its mean value using a detrend function. As the measurements obtained from the 3211 input signal cover a slightly higher frequency range with high coherence, these datasets are filtered at a cut-off frequency of 10 Hz.

For the characterisation of the phugoid motion, the measured oscillation signals in airspeed and pitch angle are used. The datasets generated by the pulse inputs are also filtered using a 5$^{\text{th}}$-order butterworth filter with a cut-off frequency of 6 Hz to reduce measurement noise. Since the TPR method requires the deviations of the measurement data around zero, the corresponding trim values are subtracted from the measured airspeed and pitch angle. A time delay of 0.08 s is considered in all datasets to account for delays due to actuator dynamics and signal processing within the Pixhawk flight control unit.

Except where otherwise noted, content of this paper is licensed under a Creative Commons Attribution 4.0 International License.

The reproduction and distribution with attribution of the entire paper or of individual pages, in electronic or printed form, including any material under non-CC-BY 4.0 licenses is hereby granted by the authors and respective copyright owners.

4.2 Short-Period Dynamics Identification

For the grey-box identification to identify the short-period dynamics, the commanded elevator deflections δ_e are defined as input signal. The elevator actuator was calibrated under unloaded conditions. However, given its high torque of 2 Nm and the backlash-free installation of the control surface, aerodynamic loads are expected to cause negligible deviations from the commanded deflections within the investigated airspeed range.

To capture the aircraft response, the outputs of the short-period model, as defined in Eq. (3), need to be expressed in terms of the available measurement signals. In particular, the vertical acceleration in body axes $a_{z,S}$, measured by the accelerometer, and the pitch rate q are considered. The derived pitch acceleration $\dot{q}$ is provided as additional output to improve the estimation of the parameter $c_{m\delta_e}$. As the accelerometer is not located at the aircraft's centre of gravity, it additionally measures accelerations due to rotational and centrifugal accelerations [3]. Assuming no roll and yaw motions during longitudinal manoeuvrers, the acceleration $a_{z,S}$ measured by the acceleration sensor is given by

$$a_{z,S} = a_{z,CG} - \dot{q}x_{SCG} - q^2 z_{SCG}. \tag{10}$$

Due to the small vertical distance z_{SCG} between the sensor and the centre of gravity on the UAV, the centrifugal acceleration is neglected. Thus, the acceleration $a_{z,CG}$ depends on the measured sensor acceleration $a_{z,S}$ and the position x_{SCG} of the sensor relative to the aircraft's centre of gravity along the longitudinal axis. Accordingly, the output equation of the short-period model in Eq. (3) is adapted to the available measurements by

$$\begin{bmatrix} a_{z,S} \\ q \\ \dot{q} \end{bmatrix} = \begin{bmatrix} Z_\alpha V^* - M_\alpha x_{SCG} & Z_q V^* - M_q x_{SCG} \\ 0 & 1 \\ M_\alpha & M_q \end{bmatrix} \begin{bmatrix} \alpha \\ q \end{bmatrix} + \begin{bmatrix} Z_{\delta_e} V^* - M_{\delta_e} x_{SCG} \\ 0 \\ M_{\delta_e} \end{bmatrix} \delta_e. \tag{11}$$

To estimate the parameters of the short-period dynamics, the available test data from at least five chirp input signals are processed simultaneously to obtain a single set of parameter values for each airspeed tested. Applying the prediction error optimisation algorithm, parameter boundaries are specified to ensure physically meaningful values. In particular, the optimisation algorithm tended to converge to excessively high values for $c_{L\alpha}$. Consequently, the parameter is constrained to a value of 4.7 based on aerodynamic calculations and wind tunnel test results [16]. The resulting estimated parameter values for the linear short-period model across the airspeeds are listed in Table 2. As criterion for their accuracy, the standard deviations of the estimators are derived from the covariance matrix P of the estimated parameters. The parameter error covariance is approximated via the Fisher information matrix [3]. The diagonal elements p_{ii} of the covariance matrix P correspond to the variances of the estimates providing a measure of their uncertainty. The standard deviation of an estimated parameter Θ_i is calculated by $\sigma_{\theta_i} = \sqrt{p_{ii}}$. Based on this, a 95% confidence interval for the parameters is determined using the normal distribution

$$95\%\ \text{CI} = \Theta_i \pm 1.96\sigma_{\theta_i}. \tag{12}$$

Consequently, smaller confidence intervals indicate greater statistical accuracy of the estimates. The uncertainty regarding the accuracy of the estimated parameter $c_{m\delta_e}$ in terms of its absolute value is the smallest, as listed in Table 2. This is a consequence from including the pitch acceleration $\dot{q}$ as an additional output signal, which provides supplementary information about the influence of this parameter. The estimated values of the parameters c_{Lq} and $c_{L\delta_e}$ are subject to the greatest uncertainty, with a maximum of 16 % relative to their absolute values. However, based on experience, this level of uncertainty is acceptable for control system design purposes as a robust flight controller can still accommodate parameter variations in this range.

Except where otherwise noted, content of this paper is licensed under a Creative Commons Attribution 4.0 International License.

The reproduction and distribution with attribution of the entire paper or of individual pages, in electronic or printed form, including any material under non-CC-BY 4.0 licenses is hereby granted by the authors and respective copyright owners.

Table 2 Short-period parameter estimation results at airspeeds of 15 m/s, 20 m/s, and 25 m/s

Parameter	Value for 15 m/s	95% CI	Value for 20 m/s	95% CI	Value for 25 m/s	95% CI
$c_{L\alpha}$	4.7	±0.205	4.7	±0.124	4.7	±0.256
c_{Lq}	0.292	±0.038	0.220	±0.020	0.317	±0.035
$c_{L\delta_e}$	0.765	±0.097	0.691	±0.074	1.082	±0.177
$c_{m\alpha}$ v	-1.832	±0.059	-1.618	±0.034	-1.670	±0.067
c_{mq}	-0.259	±0.005	-0.173	±0.003	-0.193	±0.005
$c_{m\delta_e}$	-1.242	±0.011	-1.140	±0.006	-1.268	±0.010

Next, to evaluate the quality of the identified model, fitness values for each output are calculated based on the Normalised Root Mean Square Error

$$f_y(\%) = 100\left(1 - \frac{\|y - \hat{y}\|_2}{\|y - \bar{y}\|_2}\right), \tag{13}$$

with the measured output y from the flight tests, the predicted output $\hat{y}$ from the identified model, and the mean of the experimental data $\bar{y}$. A fitness of 100% indicates a perfect match with the measurements, while 0% implies the model performs no better than the mean of the data. The diagrams in Fig. 3 compares the measured acceleration a_z and the pitch rate q with the model response for the identification test case at 15 m/s. The model responses (——) closely match the measured data (——) suggesting that the identified model provides an adequate representation of the short-period dynamics for the examined flight condition.

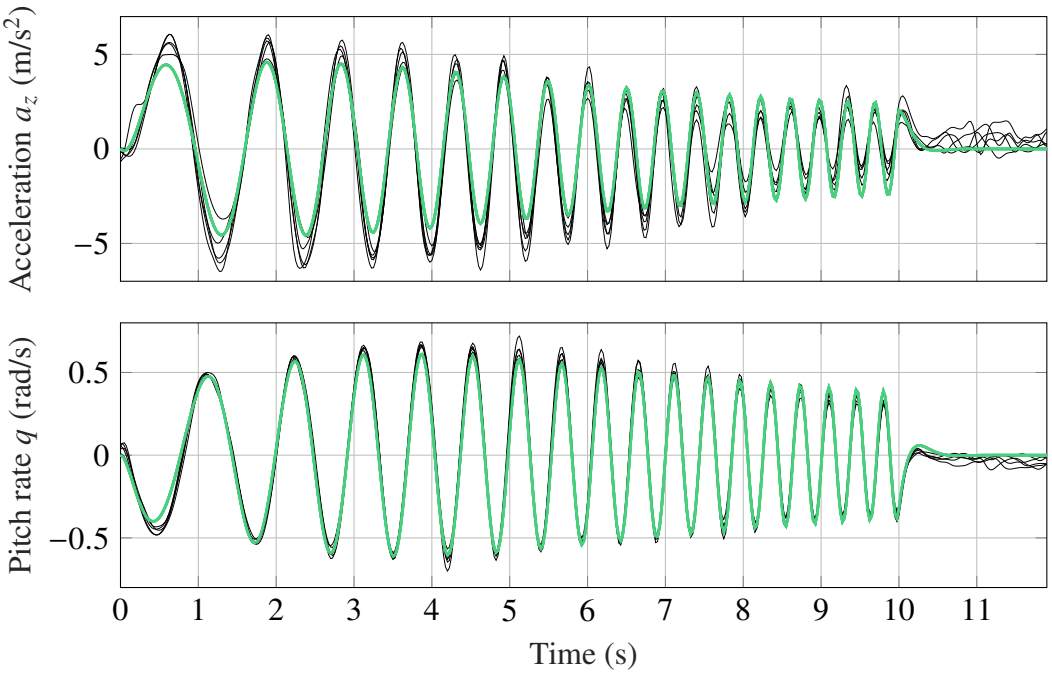

Fig. 3 Comparison between the measured data (——) and the simulated model response with the identified parameter values (——) from chirp input commands at an airspeed of 15 m/s

The diagrams indicate that the estimated model better captures the measured pitch rate than the acceleration. This is due to a stronger influence of external disturbances on the measured acceleration. The fitness values for these two cases are 70.8% for the vertical acceleration and 87.2% for the pitch rate. The diagrams also confirm that the eigenfrequency of the short-period dynamics is correctly captured by

Except where otherwise noted, content of this paper is licensed under a Creative Commons Attribution 4.0 International License.

The reproduction and distribution with attribution of the entire paper or of individual pages, in electronic or printed form, including any material under non-CC-BY 4.0 licenses is hereby granted by the authors and respective copyright owners.

the estimated model, which is of great importance for the design of flight controllers. Similar results are observed for the identification test cases at airspeeds of 15 m/s and 25 m/s. In both cases, the identified model slightly underestimates the amplitude of the vertical acceleration.

The quality of the identified short-period models is further validated by means of independent test data to ensure that the models accurately represent the studied aircraft dynamics beyond the measurements used for the parameter estimation. Thus, the 3211 input signals are applied to the models using the previously identified parameters and the resulting responses are compared to the recorded measurements in flight. Fig. 4 depicts this comparison for the 3211 validation test case at an airspeed of 15 m/s. The model response closely matches the experimental measurements with satisfactory fitness values of 59.6 % for vertical acceleration and 63.3 % for pitch rate. The lower signal to noise ratio of the 3211 input signal compared to the chirp signal is identified to cause the slight reduction of fitness values.

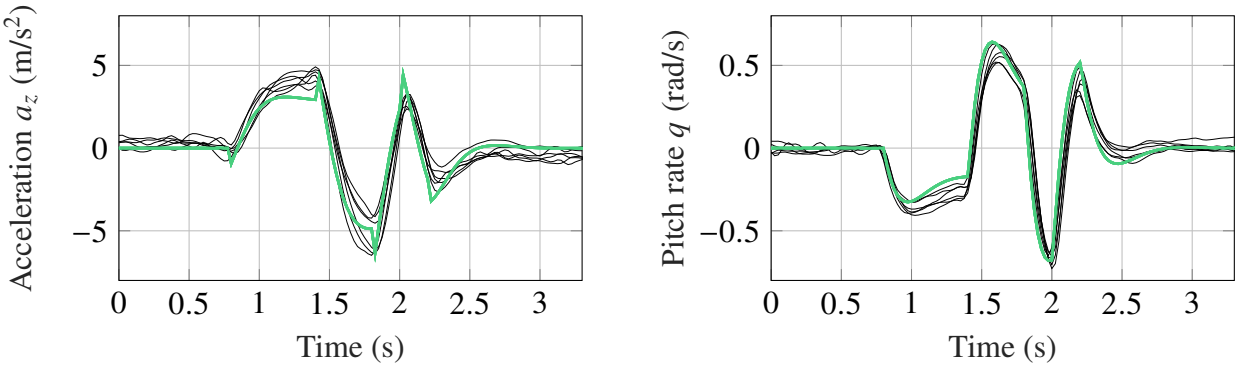

Fig. 4 Comparison between the simulated model response with the identified parameter values (——) and the measured data (——) for the 3211 validation test case at an airspeed of 15 m/s

The achieved fitness values for the short-period dynamics in both the identification and validation test cases across the examined airspeeds are summarised in Table 3. For the identification chirp test cases, consistently high fitness values, exceeding 70% and reaching up to 90%, indicate a strong compatibility between the model and the experimental measurements across all airspeeds. Again, the lowest fitness values are observed for the vertical acceleration output due to the aforementioned increased sensitivity to external disturbances. The fitness values for the 3211 validation test case range from 59% up to 70% and confirm that the obtained models provide an accurate representation of the aircraft's pitching dynamics.

Table 3 Fitness values for identification and validation test cases

Airspeed (m/s)	15	20	25
Identification chirp fitness values (%)			
Acceleration output a_z	70.8	69.3	75.1
Pitch rate output q	87.2	87.7	90.3
Validation 3211 fitness values (%)			
Acceleration output a_z	59.6	64.8	61.7
Pitch rate output q	63.3	69.3	70.6

Finally, using the short-period models identified from flight test data, the resulting natural frequency ω_n and damping ratio ζ are derived and compared across the examined airspeed range. The results for the natural frequency (◊) and the damping ratio (○) are provided in the left diagram of Fig. 5 for the three reference airspeeds of 15 m/s (——), 20 m/s (——) and 25 m/s (——). The natural frequency of the short-period model at the aircraft's cruise speed of 15 m/s is approximately 1.3 Hz, which is close to the initial estimate of 1.1 Hz based on previous AVL calculations. As expected, the natural frequency

Except where otherwise noted, content of this paper is licensed under a Creative Commons Attribution 4.0 International License.

The reproduction and distribution with attribution of the entire paper or of individual pages, in electronic or printed form, including any material under non-CC-BY 4.0 licenses is hereby granted by the authors and respective copyright owners.

increases across the examined airspeed range. The identified models reveal high damping ratios between 0.65 and 0.8, reflecting well-damped short-period behavior. The right diagram of Fig. 5 visualizes the resulting short-period motion eigenvalues $\lambda_{1,2} = -\omega_n\zeta \pm \sqrt{\omega_n^2(\zeta^2 - 1)}$ via their real and imaginary part for the three reference airspeeds. Again the pronounced increase in frequency and rather constant damping value with an increase in airspeed is clearly visible. Note that due the symmetry around the x-axis, only the positive side of the y-axis is shown.

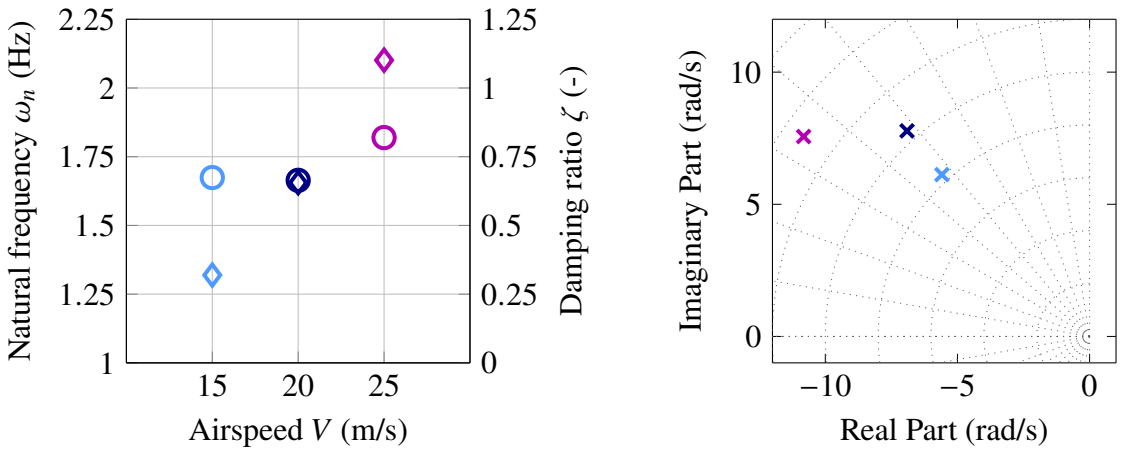

Fig. 5 Natural frequency (◊), damping ratio (○) and eigenvalues (×) of the identified short period models for the examined airspeeds of 15 m/s (——), 20 m/s (——) and 25 m/s (——)

4.3 Phugoid Motion Identification

The phugoid motion of the studied aircraft has been excited successfully by commanded elevator pulses. As depicted in Fig. 6, a typical oscillation of the measured airspeed and pitch angle is observed in the low-frequency range, while pitch rate and vertical acceleration quickly return to zero. Due to the chosen energy level of the elevator pulse, the change in airspeed in the test case of 15 m/s reaches a maximum amplitude of 2 m/s. Slightly higher amplitudes are encountered at higher trim speeds.

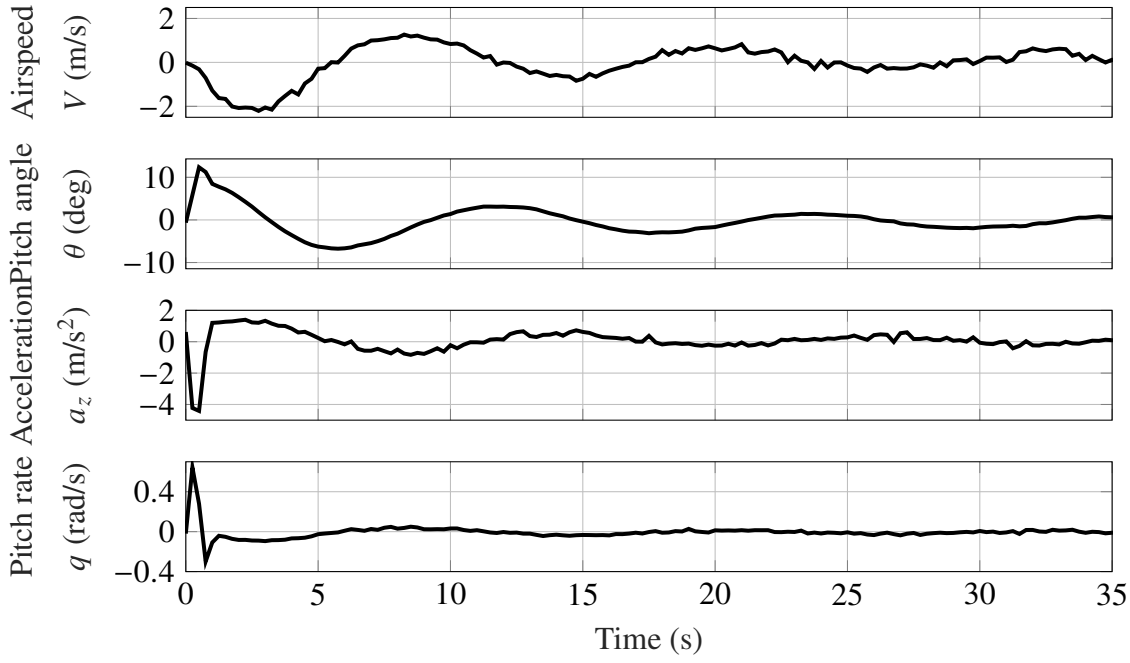

Fig. 6 Measured flight data due to an elevator pulse excitation of 0.5 s and -30° at 15 m/s airspeed

Except where otherwise noted, content of this paper is licensed under a Creative Commons Attribution 4.0 International License.

The reproduction and distribution with attribution of the entire paper or of individual pages, in electronic or printed form, including any material under non-CC-BY 4.0 licenses is hereby granted by the authors and respective copyright owners.

Using the TPR method, the oscillation period, natural frequency and damping ratio of the phugoid mode excited in flight are estimated from the measurement data. The results are summarised in Table 4. Since the aircraft has to remain visible from the ground throughout the flight, no complete oscillation cycle after the pulse input signal could be recorded in the test case at 25 m/s before the aircraft had to change its course. Consequently, a reliable estimation of the natural frequency and damping ratio based on the TPR method is not possible for this test case.

As the trim speed increases, the oscillation period of the observed phugoid motion is longer. In the test case of 15 m/s, the period is approximately 12 s and increases to 17 s at a trim speed of 20 m/s. The derived damping ratios also increase across the investigated airspeed range. It should be noted that the damping values are highly affected by any variations in thrust. Although the PWM signal controlling the motor is kept constant during the phugoid manoeuvres, the thrust changes with airspeed. Since the thrust characteristics of the studied aircraft have not yet been examined, effects of this coupling are not considered in the derived values.

Table 4 Phugoid pole derived from flight test data at airspeed of 15 m/s and 20 m/s

Airspeed (m/s)	15	20
Oscillation period T (s)	12.0	16.8
Natural frequency ω_n (rad/s)	0.523	0.388
Damping ratio ζ (-)	0.070	0.199

4.4 Gliding-based Drag Coefficient Identification

The measurement data of steady aircraft performance tests are used to obtain drag coefficients and glide ratio. Gliding flights are conducted by turning the motor off and applying constant elevator deflections reaching from $-1°$ to $-12°$. During these flights a relatively constant airspeed, depending on the commanded elevator deflection, is maintained while altitude decreases linearly. Subsequently, for each gliding flight, the corresponding altitude change is calculated, and the mean value of measured airspeed and pitch angle is determined. The glide angle γ_{glide} results from the relation

$$\gamma_{\text{glide}} = \arcsin\left(\frac{\Delta h}{V_{\text{glide}}\Delta t}\right), \tag{14}$$

where the ratio $\Delta h/\Delta t$ is the descent rate computed from the measured altitude change Δh during the corresponding time interval Δt and V_{glide} is the gliding speed. Glide ratio E and drag coefficient c_D are calculated using Eq. (6) and Eq. (7), respectively. The corresponding angle of attack α is derived from the calculated glide angle γ_{glide} and the measured pitch angle θ by

$$\alpha = \gamma_{\text{glide}} + \theta. \tag{15}$$

The resulting drag coefficient as function of the angle of attack is shown in the left diagram of Fig. 7 (—■—) and compared to the results of previous wind tunnel tests (—●—), see [16]. In the wind tunnel, the aircraft has been tested at a constant airspeed of 20 m/s. Similar to the gliding flights, the propeller has been rotating at idle speed. At small angles of attack, where the parasite drag is predominant, the drag coefficients derived from flight tests closely match the wind tunnel test results. Due to the uncertainty of blockage correction in wind tunnel measurements, the difference between the drag coefficients increases at higher angles of attack. The slope of the drag coefficient corresponds to the aerodynamic parameter $c_{D\alpha}$. Using the flight test data, the value of $c_{D\alpha}$ is computed for the three trim airspeeds considered herein. Increasing with the angle of attack, and thus decreasing with the trim airspeed, $c_{D\alpha}$ takes values of 0.54 rad^{-1} at a reference airspeed of 15 m/s, 0.39 rad^{-1} at 20 m/s, and 0.31 rad^{-1} at 25 m/s.

Except where otherwise noted, content of this paper is licensed under a Creative Commons Attribution 4.0 International License.

The reproduction and distribution with attribution of the entire paper or of individual pages, in electronic or printed form, including any material under non-CC-BY 4.0 licenses is hereby granted by the authors and respective copyright owners.

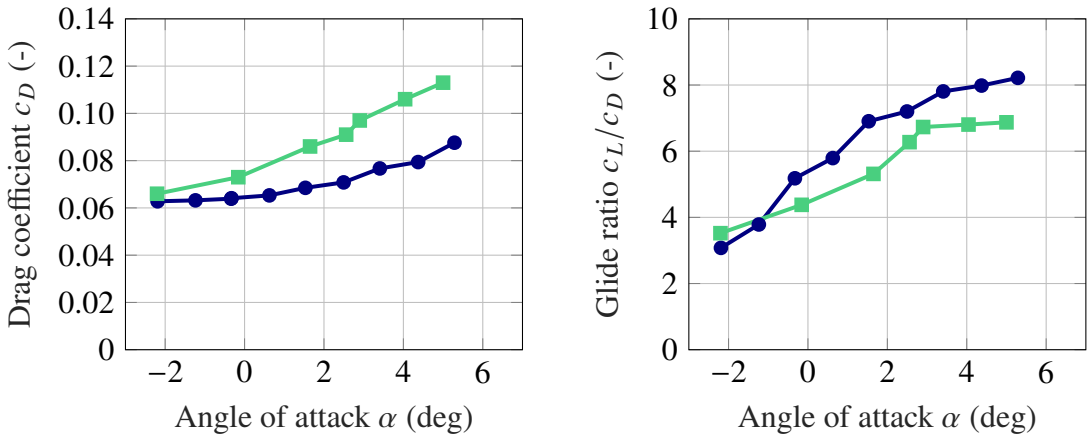

Fig. 7 Drag coefficient and glide ratio measured during gliding flight (—■—) and in the wind tunnel (—●—)

The glide ratio derived from measurements increases with higher angles of attack across the examined airspeed range, as depicted in the right diagram of Fig. 7. The values obtained in flight are slightly lower than those measured in the wind tunnel. Due to the propeller rotating at idle, the measurements from both test campaigns are not suitable for determining the maximum glide ratio and hence the optimal cruise speed because the additional drag produced by the propeller is compensated in cruise by motor thrust. Nevertheless, the derived glide ratios are essential for estimating the remaining gliding distance in the event of an engine failure and thus, gaining further insight into the longitudinal behaviour of the aircraft. Within the investigated airspeed range, the maximum lift-to-drag ratio obtained in flight is achieved at an angle of attack of approximately 5° corresponding to an airspeed of 15 m/s.

5 Conclusion

For the small fixed-wing UAV Urban Condor X, a flight test campaign is described, allowing to characterise the aircraft's longitudinal motion over its operational airspeed range. Measurement data recorded by a Pixhawk 6x control unit is used to follow a combined identification approach: Applying grey-box methods, the parameters of a separated linear state-space model for short-period dynamics are identified, while the eigenmode characteristics of the phugoid dynamics are derived from transient response analysis. Drag coefficients determined from gliding flight data confirm previous wind tunnel test results, taking the influence of the rotating propeller into account. The resulting short-period models across the examined airspeed range are consistent with the measurements and exhibit plausible natural frequencies and damping ratios. The parameter values derived from a-priori models served as initial estimates for the grey-box identification, ensuring adequate accuracy in the nested optimization process. The resulting identified parameters can now be used to refine these models and enhance the future design of control systems. The presented results thus successfully validate the mathematical model development chain for small fixed-wing unmanned aerial vehicles, i.e., from the initial approximation to flight test validation.

Acknowledgments

This research was funded by the German Federal Ministry for Digital and Transport under grant number 19F1176A. The responsibility for the content of this paper is with its authors. The financial support is gratefully acknowledged.

Except where otherwise noted, content of this paper is licensed under a Creative Commons Attribution 4.0 International License.

The reproduction and distribution with attribution of the entire paper or of individual pages, in electronic or printed form, including any material under non-CC-BY 4.0 licenses is hereby granted by the authors and respective copyright owners.

Declaration of Use of Artificial Intelligence

Artificial intelligence was not used in the work presented.

References

[1] Hazim Shakhatreh, Ahmad H. Sawalmeh, Ala Al-Fuqaha, Zuochao Dou, Eyad Almaita, Issa Khalil, Noor Shamsiah Othman, Abdallah Khreishah, and Mohsen Guizani. Unmanned Aerial Vehicles (UAVs): A Survey on Civil Applications and Key Research Challenges. *IEEE Access*, 7:48572–48634, 2019. doi: 10.1109/access.2019.2909530.

[2] Andrei Dorobantu, Austin Murch, Bérénice Mettler, and Gary Balas. System Identification for Small, Low-Cost, Fixed-Wing Unmanned Aircraft. *Journal of Aircraft*, 50(4):1117–1130, 2013. doi: 10.2514/1.c032065.

[3] Ravindra V. Jategaonkar. *Flight Vehicle System Identification: A Time-Domain Methodology*. American Institute of Aeronautics and Astronautics, 2nd edition, 2015. ISBN: 978-1624102783. doi: 10.2514/4.102790.

[4] Vladislav Klein and Eugene A. Morelli. *Aircraft System Identification: Theory and Practice*. AIAA education series. American Institute of Aeronautics and Astronautics, Reston, VA, 2006. ISBN: 978-1563478321.

[5] Nathan V. Hoffer, Calvin Coopmans, Austin M. Jensen, and YangQuan Chen. A Survey and Categorization of Small Low-Cost Unmanned Aerial Vehicle System Identification. *Journal of Intelligent & Robotic Systems*, 74:129–145, 2014. doi: 10.1007/s10846-013-9931-6.

[6] Bogdan Løw-Hansen, Richard Hann, Kristoffer Gryte, Tor Arne Johansen, and Christoph Deiler. Modeling and identification of a small fixed-wing UAV using estimated aerodynamic angles. *CEAS Aeronautical Journal*, 16(2):501–523, 2025. doi: 10.1007/s13272-025-00816-3.

[7] Stephen Carnduff. *System Identification of Unmanned Aerial Vehicles*. PhD thesis, Cranfield University, Cranfield, United Kingdom, 2008.

[8] Benjamin M. Simmons, James L. Gresham, and Craig A. Woolsey. Flight-Test System Identification Techniques and Applications for Small, Low-Cost, Fixed-Wing Aircraft. *Journal of Aircraft*, 60(5):1503–1521, 2023. doi: 10.2514/1.c037260.

[9] Ony Arifianto and Mazen Farhood. Development and Modeling of a Low-Cost Unmanned Aerial Vehicle Research Platform. *Journal of Intelligent & Robotic Systems*, 80(1):139–164, 2015. doi: 10.1007/s10846-014-0145-3.

[10] David J. Grymin and Mazen Farhood. Two-Step System Identification and Trajectory Tracking Control of a Small Fixed-Wing UAV. *Journal of Intelligent & Robotic Systems*, 83(1):105–131, 2016. doi: 10.1007/s10846-015-0298-8.

[11] Nuno M. B. Matos and André C. Marta. Longitudinal Motion System Identification of a Fixed-Wing Unmanned Aerial Vehicle Using Limited Unplanned Flight Data. *Aerospace*, 11:959, 2024. doi: 10.3390/aerospace11120959.

[12] Lennart Ljung. *System Identification: Theory for the User*. Prentice Hall Information and System Sciences Series. Prentice Hall PTR, Upper Saddle River, NJ, 2nd edition, 1999. ISBN: 978-0136566953.

[13] Thomas R. Yechout, Steven L. Morris, David E. Bossert, and Wayne F. Hallgren. *Introduction to Aircraft Flight Mechanics*. AIAA Education Series. American Institute of Aeronautics and Astronautics, Reston, VA, 2003. ISBN: 978-1563475771.

[14] Michael V. Cook. *Flight Dynamics Principles*. Elsevier Aerospace Engineering Series. Butterworth-Heinemann, Waltham, MA, 3rd edition, 2013. ISBN: 978-0080982762.

Except where otherwise noted, content of this paper is licensed under a Creative Commons Attribution 4.0 International License.

The reproduction and distribution with attribution of the entire paper or of individual pages, in electronic or printed form, including any material under non-CC-BY 4.0 licenses is hereby granted by the authors and respective copyright owners.

[15] M. Drela and H. Youngren. *Athena Vortex Lattice 3.36*. Massachusetts Institute of Technology, 2017.

[16] Sabine Wisbacher, Daniel Ossmann, Sebastian Schubert, Jürgen Frey, and Harald Pfifer. Wind Tunnel Based System Identification of a Small Unmanned Aircraft System. In *AIAA SciTech 2025 Forum*, Orlando, FL, 2025. doi: 10.2514/6.2025-0857.

Except where otherwise noted, content of this paper is licensed under a Creative Commons Attribution 4.0 International License.

The reproduction and distribution with attribution of the entire paper or of individual pages, in electronic or printed form, including any material under non-CC-BY 4.0 licenses is hereby granted by the authors and respective copyright owners.